Effect of Higher Carrier Mobility of the Reduced Graphene Oxide−Zinc Telluride Nanocomposite on Efficient Charge Transfer Facility and the Photodecomposition of Rhodamine B

Dhananjoy Das,[§] Mainak Das,[§] Sayantan Sil,[§] Puspendu Sahu,[§] and Partha Pratim Ray*,[§]

Read Online

ACCESS | Metrics & More | Article Recommendations | SI Supporting Information

ABSTRACT: The synthesis of solar-light-responsive zinc telluride (ZnTe) nanoparticles and their composite with reduced graphene oxide (rGO−ZnTe) via a simple hydrothermal reaction is reported. The synthesized nanostructures were comprehensively character-ized by a combination of X-ray diffraction and photoelectron spectroscopy, electron microscopy, UV−vis spectroscopy, photo-luminescence spectroscopy and thermogravimetric analysis. The effects of graphene oxide on the crystallinity, microstructure, photo-excitation, light absorption, surface area and thermal stability of ZnTe were studied. The current−voltage $(I−V)$ characteristics for both as-synthesized ZnTe and rGO−ZnTe composite-based Schottky devices were measured to estimate the charge transport

parameters such as dc conductivity, photosensitivity, carrier's mobility and lifetime. The photocatalytic performance of both the materials in the degradation of an azo dye (Rhodamine B) was subsequently investigated using simulated solar light. The rGO− ZnTe composite exhibited a higher photocatalytic activity (66%) as compared to the as-synthesized ZnTe (23%), essentially due to the synergy between rGO sheets and ZnTe nanoparticles. The role of the carrier's mobility in the transportation of photo-induced charges (electrons and holes) through the complex network of the composite materials and thus facilitating the photo-degradation process is explained. In the end, the responsible reactive species for the decomposition of Rhodamine B was also interpreted.
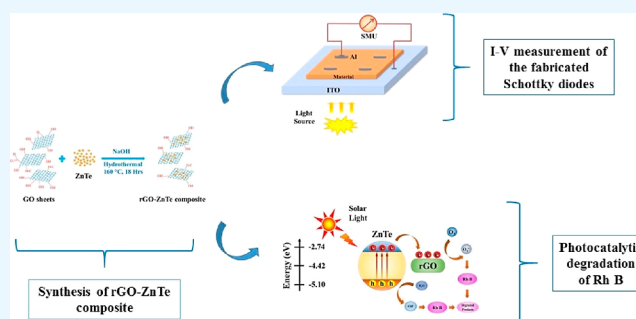
INTRODUCTION

Dye wastewater released into water bodies mainly by textile industries is becoming a major environmental concern, causing several ecological problems.[1] In the past few decades, different physicochemical and biological attempts based on chemical and physical adsorption techniques have been made to degrade these industrial effluents, but they are not cost-effective from an economical point of view and often produce secondary pollutants.[2] Among all advanced oxidation methods known to date, the photocatalytic route based on semiconducting materials has shown considerable efficiency in wastewater decontamination processes.[3] Thus far, a large number of compound semiconductors have been investigated for organic dye decomposition since they possess an excellent larger absorbance cross-section and higher environmental stability.[4] Although the semiconductor materials have excellent potential in the area of organic dye decolorization, they suffer from the shortcomings of having wide band gaps and a comparatively shorter life span of excitons, limiting the usage of these semiconductors in practical applications.[5] As an example, TiO$_2$, which is one of the most promising materials for the decomposition of many organic pollutants, responds only in the UV region of the electromagnetic spectrum, attributed to its wide band gap (∼3.2 eV).[6] This causes fewer redox

reactions with the pollutants and detrimentally affects its degradation efficiency.[7]

On the other hand, zinc telluride (ZnTe), which is an important group II−VI compound semiconductor having a direct band gap of ∼2.26 eV, has shown immense potential in a wide range of applications in solar cells,[8] light-emitting diodes,[9] optoelectronic devices,[10] CO$_2$ reductions,[11] and in wastewater treatment.[12] The solution-processed ZnTe nanostructures demonstrate a few excellent features, namely, low production cost, large surface area, good environmental stability, excellent reusability and prominent visible-light absorption, which make them a prospective photocatalyst. However, they also have an inherent shortcoming that the fast electron (e$^-$)−hole (h$^+$) recombination in ZnTe nanomaterials is responsible for their weak photocatalytic performance, particularly under visible light irradiation. Several attempts were made to decrease the electron−hole recombination in these materials and thus

Scheme 1. Schematic Illustration of the Synthesis of the rGO−ZnTe Nanocomposite

promote the electron transfer during the photocatalytic process. Among them, the synthesis of graphene-based composites is considered as one of the most effective remedial techniques,[13] wherein the easily processed, low-cost graphene oxide (GO) and/or reduced GO (rGO) possess high specific surface area alongside manifesting superior conductivity.[14] The presence of different functional groups further allows the GO sheets to exfoliate easily in water and thereby produce stable dispersions. These exfoliated GO sheets owing to possessing a large surface area also provide sufficient interfacial contact with the nanoparticles, which, in turn, suppress the recombination of photo-generated electron−hole pairs and thereby enhance the charge transfer facility.[15] The present work describes the synthesis of the reduced graphene oxide−zinc telluride (rGO−ZnTe) nanocomposite and identifies their potential in the degradation of organic dye [Rhodamine B (RhB)] under visible light irradiation. The associated enhancement in the transport properties of the charge carriers and the role of their mobility in dye degradation are discussed in detail in this report.

EXPERIMENTAL SECTION

Materials. The chemicals used in this study were zinc (Zn) powder (assay ≥93%), tellurium (Te) powder (∼30 mesh, 99.997%), sodium hydroxide (NaOH) (analytical grade, >97%), graphite powder (98%), H_2SO_4, H_3PO_4, $KMnO_4$, H_2O_2, HCl, absolute ethanol and deionized (DI) water. All the reagents were purchased from Sigma-Aldrich (India) and utilized without any further purification.

Synthesis of ZnTe. ZnTe (ZT) nanoparticles were synthesized by the hydrothermal (HT) route, as reported previously.[16] In a typical HT method, 0.36 g of Zn powder, 0.66 g of Te powder and 1.61 g of NaOH pellets were dissolved into 40 mL of DI water, and a homogeneous solution was obtained after magnetically stirring for 2 h. The solution was then put into a Teflon-lined HT autoclave, and additional DI water was added for dilution. Thereafter, the autoclave was placed inside an oven with a heat flow rate of 3 °C/min, and the thermal treatment was executed at a constant temperature of 160 °C for 18 h. Subsequently, the autoclave was cooled down to room temperature, and the resulting gray-colored ZT sediment was then collected using the centrifugation technique following repetitive washing using DI water and absolute ethanol. Finally, the as-synthesized ZT nanoparticles were dried overnight in a vacuum furnace at 80 °C.

Synthesis of GO. GO was synthesized using improved Hummer's method, first proposed by Marcano et al.[17] Briefly, a 100 mL solution of H_2SO_4/H_3PO_4 with a molar ratio of 9:1 was prepared, and 0.75 g of graphite flakes was dispersed into it with strong sonication. Next, 4.5 g of $KMnO_4$ was gradually introduced to the acid suspensions and was continuously stirred for 12 h at 50 °C. The homogeneous mixture was then cooled down to room temperature and transferred to 100 mL of ice water. Next, 0.75 mL of aqueous solution (30%, v/v) of H_2O_2 was slowly added to the homogeneous mixture, and a golden−brown suspension of GO was obtained. After filtration and centrifugation (6000 rpm, 1 h), the resulting GO was repeatedly rinsed with DI water, dilute HCl and ethanol. Finally, the product was obtained after overnight drying at 100 °C.

Synthesis of rGO−ZnTe. The composite material rGO−ZnTe (R−ZT) with a certain weight ratio (rGO/ZT = 1:20, rGO 5 wt %) was synthesized following a similar alkaline HT reaction that was adopted to synthesize ZnTe and is described above. First, 10 mg of reduced GO was obtained from GO by the hydrazine treatment, as described by Das et al.[18] Then, 5 mg of rGO was exfoliated in 30 mL of DI water by ultrasonication for 1 h, and a well-dispersed homogeneous solution was obtained. Subsequently, the as-synthesized ZT was slowly added to the rGO suspension while maintaining the stirring. The mixture was further stirred for 1 h to prepare a uniform solution and subsequently poured into an HT autoclave to synthesize the R−ZT nanocomposite. Here, further deoxygenation of rGO and the formation of the R−ZT composite took place simultaneously in the NaOH medium.[19] The gray-colored residue collected after centrifugation was thoroughly washed and dried overnight to obtain the R−ZT nanocomposite. The entire synthesis process of the rGO−ZnTe composite is collectively schemed out in Scheme 1.

Material Characterizations. The crystal structure and the constituent phase(s) in the synthesized materials (ZT and R−ZT) were investigated by the Rietveld refinement of the X-ray diffraction (XRD) patterns acquired using a laboratory X-ray powder diffractometer (Bruker D8, Cu-Kα = 1.5418 Å) operated with a position-sensitive detector and a scan rate of 0.1°/min. The surface morphology and the elemental composition were studied with an FEI Inspect F50 field emission scanning electron microscope and an integrated energy-dispersive X-ray analyzer, respectively. The micro-structural information of the nanocomposite was analyzed
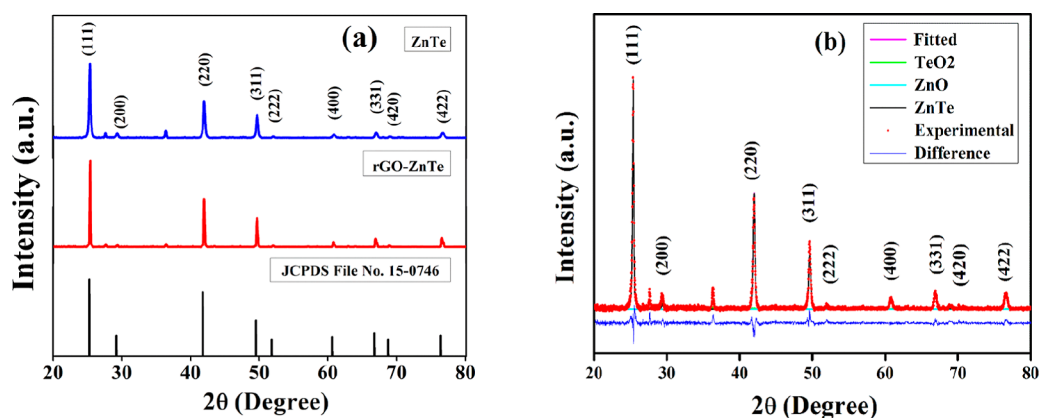
Figure 1. (a) XRD spectra of the as-synthesized ZT and R−ZT nanocomposite. (b) Rietveld refinement of the ZT specimen.
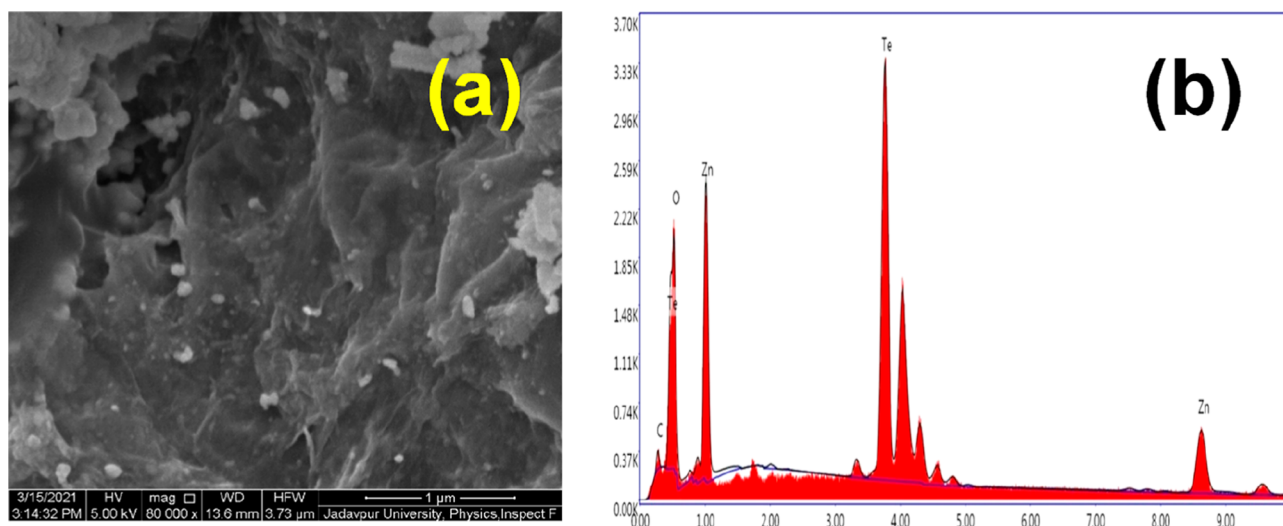

Figure 2. (a) FESEM image and (b) EDX spectra of the R−ZT nanocomposite.

using a JEOL JEM 2100F field emission gun (FEG) transmission electron microscope. The X-ray photoelectron spectroscopy (XPS) (Omicron Nanotechnology) measurement technique using Al-K$_\alpha$ radiation (E = 1486.7 eV) was employed to probe the surface electronic states of the existing elements and the reduction state of GO. The absorption spectra of synthesized materials and their photocatalytic behavior were investigated using a UV−vis spectrophotometer (PerkinElmer, Lambda 365) and a low-cost solar simulator (Abet Technologies, model 10500), respectively. The photoluminance spectra of the samples were collected using a spectrofluorometer (PerkinElmer LS55). The thermal stability of both of the materials was investigated by thermogravimetric analysis (PerkinElmer Pyris Diamond TG/DTA) in the temperature range of 25−750 °C under a N$_2$ atmosphere. For the interpretation of the Brunauer−Emmett−Teller (BET) specific surface area of the nanomaterials, the N$_2$ adsorption−desorption was performed at 77 K (Autosorb iQ2, Quantachrome Instruments, USA). The current−voltage (I−V) measurements of the ZT and R−ZT specimens were studied with the help of a semi-automated source measurement unit (Keithley 2600B).

RESULTS AND DISCUSSION

Structural Properties. Rietveld refinement of the as-synthesized ZT and R−ZT composite was carried out using the MAUD program,[20] and the fitted XRD patterns are presented in Figure 1b. Figure 1a displays the observed Bragg reflections of the as-prepared ZT specimens at $2\theta \approx 25.26$, 41.81, 49.50, 60.63, 66.74, and 76.39°, assigned to (111), (220), (311), (400), (331), and (422) crystallographic planes, respectively (JCPDS file no. 15-0746), refined according to the crystal structure of ZnTe.[11] The corresponding crystal structure is also available at Crystallography Open Database (COD) entry no. 1540103, having a space group *Fm-3m*.[21] Additionally, a pair of very weak peaks at $2\theta \approx 27.61$ and 36.27° of zinc oxide (ZnO) and tellurium dioxide (TeO$_2$), respectively, were also detected in the specimens, which have corresponding COD entry nos. 2107059 and 1520934. The incidence of these two peaks could be attributed to the residual zinc and tellurium, precipitated and oxidized during HT treatment.[22]

The quality of refinements in Figure 1b was ascertained from the "goodness of fit" parameter values lying close to unity, which is standard practice while carrying out Rietveld structure refinement. The presence of the trace amount of secondary phases is easily discernible from the deconvoluted XRD pattern in Figure 1b, presented as a representative for the pure ZT

specimen. The refinement yields a lattice constant value of $a = 6.1031$ Å for pure ZT, increasing to $a = 6.1048$ Å for the R−ZT composite, indicating an insignificant lattice expansion of ∼0.03% due to the incorporation of rGO with ZT. Interestingly, although the R−ZT composite XRD pattern in Figure 2a resembles closely that of pure ZT, including the presence of trace ZnO and TeO$_2$ phases, they reveal markedly sharp peaks, suggesting the higher crystallinity in the specimens. A further observation from Figure 1a is that the addition of rGO did not affect the relative intensities and positions of the Bragg reflections in ZT and R−ZT which could result in the growth of new crystallographic phases. Also, no characteristic diffraction peaks for rGO were noticed in the composite, which is attributed to the low level of loading and comparatively weaker diffraction peaks of GO.[23] The interplanar spacing (d) of the ZT crystal is measured from Bragg's equation ($2d \sin \theta = n\lambda$) as 3.50 Å corresponding to (111) lattice planes. The formation of GO and its reduction to rGO were authenticated by the XRD spectra of GO and rGO, displayed in Figure S2 (Supporting Information).

The morphology and microstructural information of the synthesized materials were also confirmed by electron microscopy studies. First, the field-emission scanning electron microscopy (FESEM) image presented in Figure 2a displays the distribution of ZT nanoparticles over the crumpled graphene layers in the R−ZT composite. Some random agglomeration of ZT nanoparticles is also observed, which might occur from the aggregation tendency of the graphene layers due to the van der Waals interaction.[19] The corresponding energy-dispersive X-ray spectroscopy (EDX) spectra presented alongside in Figure 2b confirm the presence of constituting elements (Zn, Te, C, and O) in the nanocomposite. Furthermore, the quantitative analysis of EDX reveals that the molar ratio of Zn to Te of the synthesized material was very close to unity, suggesting the formation of stoichiometric ZT nanoparticles.

The transmission electron microscopy (TEM) microstructures in Figure 3a,b are under different magnifications, wherein the ZT nanoparticles are nearly spherical nanometric-sized particles, and they are dispersed uniformly over the wrinkled 2D rGO layers.[24] This kind of situation would help in establishing a close interface with minimal aggregation of the particles, and an intimate bond is formed between the ZT and the rGO layers.[25] The formation of the intimate bonding between the ZT and rGO layers would assist the transfer of charge carriers and thereby should inhibit their recombination. The high-resolution TEM (HRTEM) image shown in Figure 3c corresponds to an interplanar spacing of ∼3.49 Å fringe spacing for the (111) crystallographic planes of the cubic ZT lattice, agreeing reasonably well with ∼3.50 Å obtained from the XRD analysis. Figure 3d shows the selected area electron diffraction (SAED) pattern of the ZT nanoparticles with concentric diffraction rings, indicating the polycrystalline nature of the specimen.

XPS study of the R−ZT nanostructures was performed to examine the chemical composition of the surface and the oxidation state of the metallic ions. The presence of Zn, Te, C, and O in the R−ZT nanocomposite was validated by the survey spectrum in the energy range 0−1200 eV and is shown in Figure 4a. The XPS peak of C 1s for the R−ZT composite was deconvoluted into four constituent Gaussian peaks as shown in Figure 4b, and they are centered around the binding energies 283.76, 285.07, 287.16, and 290.07 eV, which are ascribed to the C=C, C−OH, C=O, and O−C=O bonds, respectively.[26] The incidence of relatively low intense oxygenated functional groups implicates their partial elimination, besides the existence of the restored graphitic segment in the composite material.[19] This, on the one hand, has an obvious ramification that the restored graphitic layers favor the electron transfer, while on the other hand, the O$_2$-containing functional groups would incite establishing a strong interaction between the nanocomposite and the aqueous solution during the photocatalytic degradation.[27]

Figure 4c further shows the high-resolution XPS spectrum corresponding to the Zn 2p doublet. The splitting of the 23.1 eV core level into Zn-2p$_{3/2}$ and Zn-2p$_{1/2}$ levels indicates the 2$^+$ oxidation state of Zn. On the other hand, two peaks corresponding to Te are identified in Figure 4d at binding energies 573 and 583.1 eV, respectively, representing the 3d$_{5/2}$ and 3d$_{3/2}$ transitions and thereby validating the establishment of Zn−Te bonding. Additionally, it is also discernible that the two Te peaks are accompanied by a pair of small but prominent peaks corresponding to energies 576.1 and 586.8 eV, arising out of the 3d$_{5/2}$ and 3d$_{3/2}$ transitions due to the incidence of other tellurium oxides (TeO$_2$ and TeO$_3$), respectively. The existence of secondary tellurium oxides in the present study has also been confirmed in the XRD patterns fitted according to Rietveld refinement (Figure 1b), which has been accredited to the oxidation of tellurium-rich phases of ZT during the HT process.[28] Nevertheless, Baghchesara et al. reckon that these oxidation states of Te could be diminished by growing the ZT at a relatively higher temperature.[29]

Optical Properties. The UV−vis absorbance spectra of the as-synthesized ZT and R−ZT nanocomposite presented in Figure 5a were recorded in the wavelength range 200−900 nm to study their optical properties. The optical band gap (E_g) of the nano-catalysts was derived following Tauc's equation (eq S1), discussed in the Supporting Information.[30] The estimated value of the band gap of pure ZT nanoparticles using Tauc's plot (Figure 5b) was 2.11 eV, which is in good agreement with the previously reported value.[31] The broadness of the absorption band of the R−ZT composite material as compared
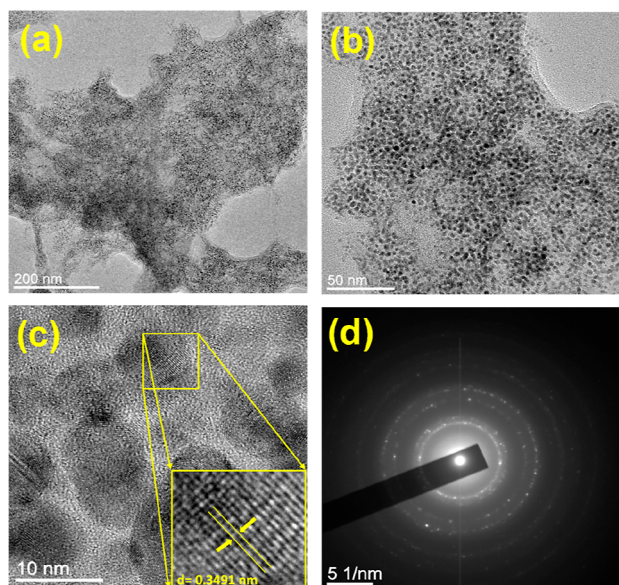

Figure 3. (a,b) TEM images of the R−ZT nanocomposite. (c) HRTEM and (d) SAED pattern of ZT nanoparticles over rGO layers.
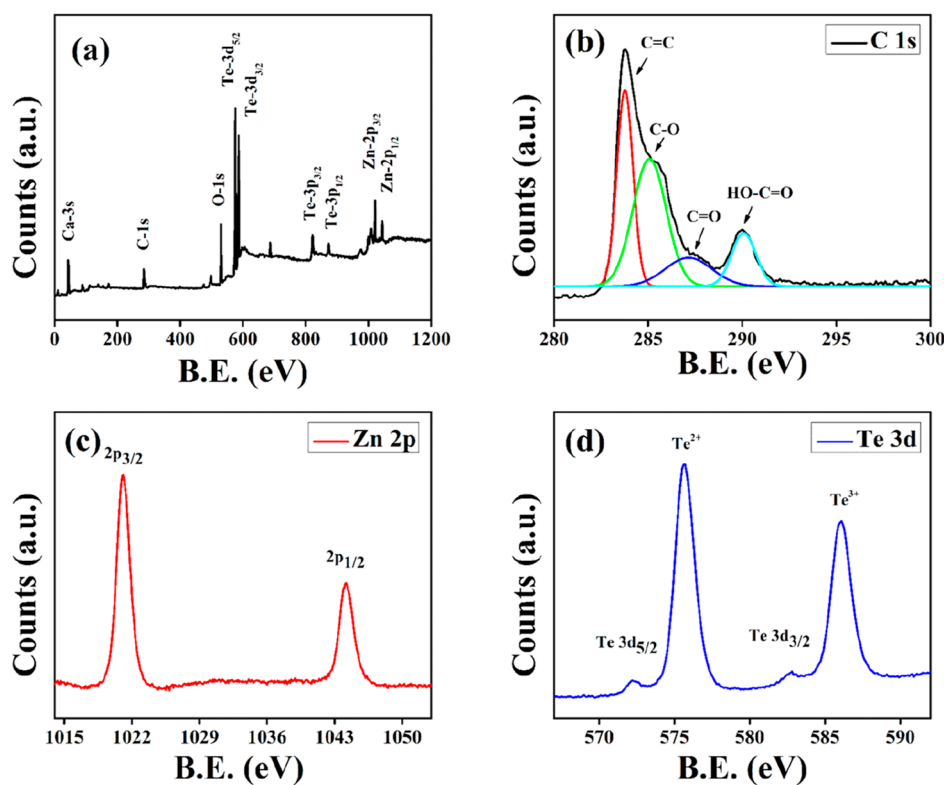
Figure 4. (a) XPS survey and (b) C 1s spectrum of the R−ZT nanocomposite. The HR-XPS spectrum of (c) Zn-2p and (d) Te-3d states.
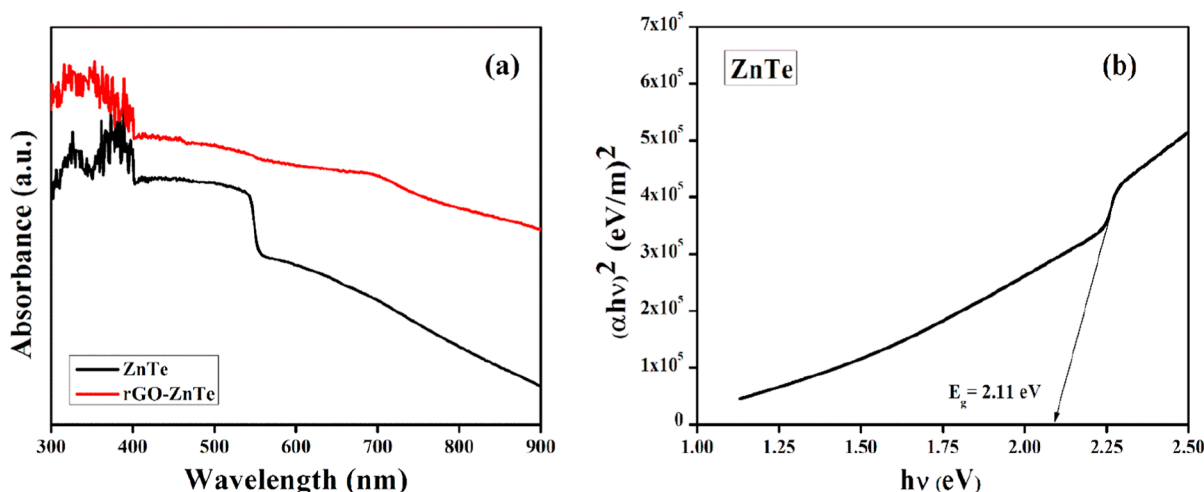

Figure 5. (a) Optical absorption spectra of the pure ZT and R−ZT composite. (b) Tauc's plot for the optical band gap of pure ZT.

to pristine ZT indicates improvement in the photon absorption and proliferation of the electron−hole pair in the photocatalytic experiment.

Photoluminescence (PL) spectroscopy is a useful tool to reveal the interaction between the electrons and holes that are generated by photon excitation. Figure 6 shows the PL spectra of the as-synthesized ZT and R−ZT nanocomposite under 315 nm excitation. The pristine ZT exhibits a prominent emission centered around 418 nm, whose intensity significantly diminishes after loading GO sheets due to the existence of strong interfacial interaction in the composite material, which renders a dedicated pathway to the electrons and holes for establishing interaction between the ZT and GO layers.[32] The electrons thus could easily migrate from the excited ZT, and

the "quenching" of fluorescence occurs. Such extended separation between the photo-generated charge carriers and their swift transportation essentially enhances the photocatalytic processes.[33]

Thermal Stability and BET Surface Area Studies. The thermal stabilities of the as-synthesized ZT and R−ZT nanocomposite were probed by thermogravimetric analysis (TGA), performed at gradual increasing temperatures (10 °C/min) from 25 to 750 °C in a N_2 atmosphere. Figure 7 depicts the TGA spectrum of the R−ZT composite, exhibiting two distinct stages of weight loss with 99.65% residue up to 700 °C. The first weight loss took place approximately at 65−185 °C, indicating the desorption of solvents and absorbed moisture, followed by a step-like second stage (435−625 °C), wherein
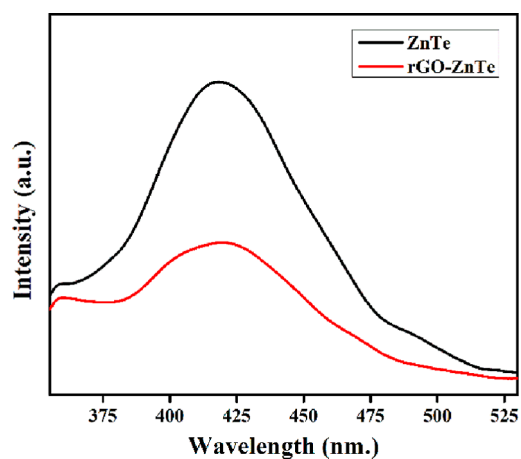
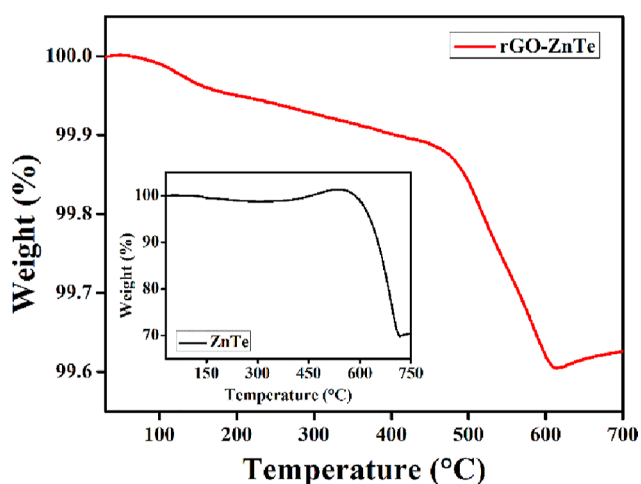**Figure 6.** PL spectra of the ZT and R−ZT nanocomposite.

Figure 7. TGA curves of the pure ZT (inset) and R−ZT nanocomposite.

the oxidation of rGO and phase transformation of ZT occur. On the other hand, the pure ZT also underwent a rapid weight loss in the temperature range of 510−715 °C, thereby leaving about 70% residue.[34] These results reveal that rGO loading imparts higher stability to the R−ZT composites, as compared to the pristine ZT.
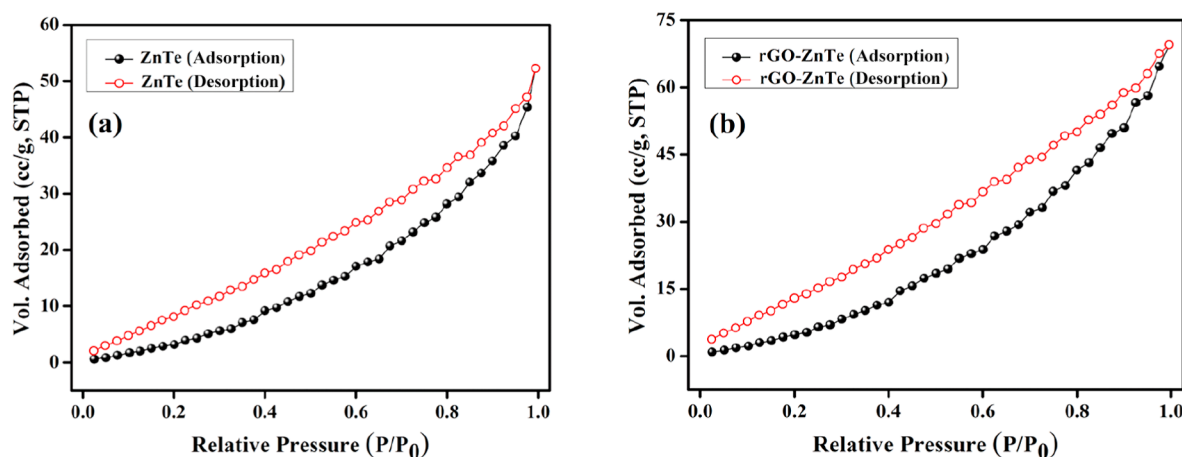
The N_2 adsorption−desorption isotherms (Figure 8) at 77 K (−196 °C) were also recorded to obtain information about the BET specific surface for the pure ZT and R−ZT nanocomposite.[35] The BET analysis estimates that the specific surface area of pristine ZT and R−ZT composites was 24.58 and 36.31 $m^2 \ g^{-1}$, respectively, expectedly indicating a higher surface area in the graphene-based composite.[11] In photocatalytic applications, a higher absorbance cross-section is always desirable since the larger the surface area, the higher will be the photo-absorption, and consequently, the diffusion of molecules is also enhanced. Figure 8, therefore, indicates that the graphene composite is expected to fulfill those requirements, which is now demonstrated in the following.

Electrical Properties. To interpret the electronic charge transport properties of the synthesized materials, the current−voltage (I−V) characteristics for the fabricated Schottky devices (Al/ZT/ITO and Al/R−ZT/ITO) (Figure S1, Supporting Information) were studied by applying a dc bias voltage of ±1 V at room temperature under dark and light (~1000 W/m^2) conditions. The dc conductivity (σ), which is a measure of the charge flow, was estimated from the linear region of the diode characteristic curves (Figure 9a) for both the devices studied under different conditions (Table 1). The significant rise in current density after light irradiation indicates the photo-responsive nature of the materials. The photo-sensitivity (S), defined as $S = I_v/I_d$, (where $I_v = I_l − I_d$ is the photo-induced current and I_d is the current under dark) was further deduced for both devices.[36] The graphene-based device, which possesses a strong absorption ability, displayed higher sensitivity than its counterpart with pristine ZT (Table 1). Also, the higher conductivity of the composite material as shown in Table 1 implies enhancement in charge transportation alongside improved mobility. For any semiconducting material, carrier mobility is very important for it decides how fast a carrier, that is, electrons and/or holes, would advance through its complex network before reaching the active sites, wherein they finally recombine with each other. Since rGO offers higher electron mobility (~$10^4 \ cm^2/V \ s$ at 300 K), it is expected to also assist their passage and electron−hole pair separation through its high-grade 2D network.[37]

To elucidate the inclusive influence of rGO on the charge transport mechanism and photodegradation process, the I−V characteristics were further analyzed by interpreting the carrier's mobility (μ_{eff}) and lifetime (τ) based on semi-

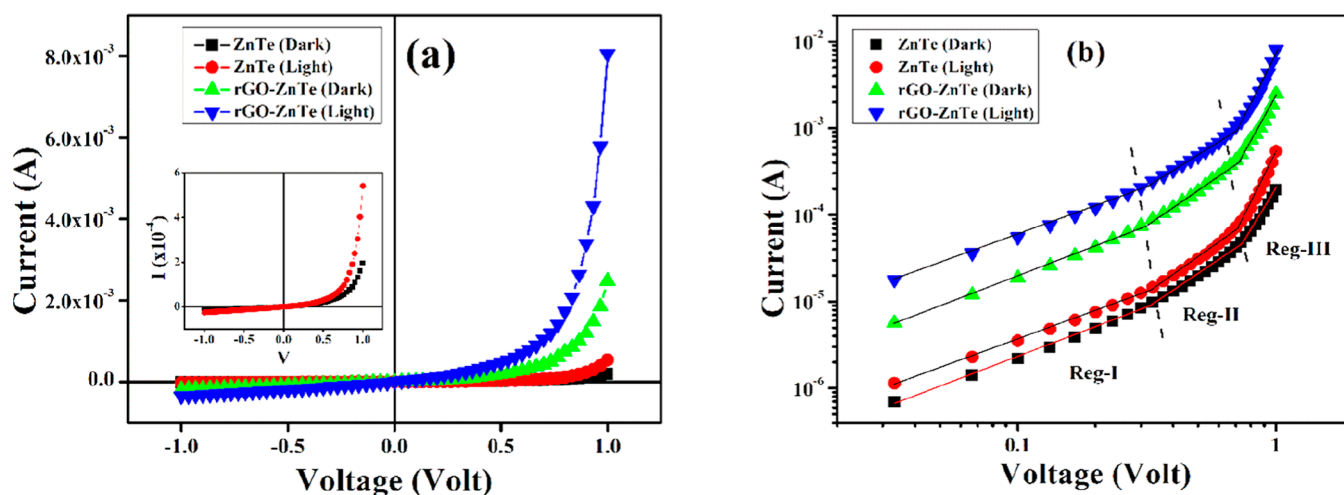**Figure 8.** N_2 adsorption−desorption isotherms for (a) ZT and (b) R−ZT nanocomposite.

Figure 9. (a) Current−voltage (I−V) characteristic curves and (b) I−V plot in the logarithmic scale for the pure ZT and R−ZT composite-based Schottky diodes under the dark and light conditions.

Table 1. Charge Transport Parameters

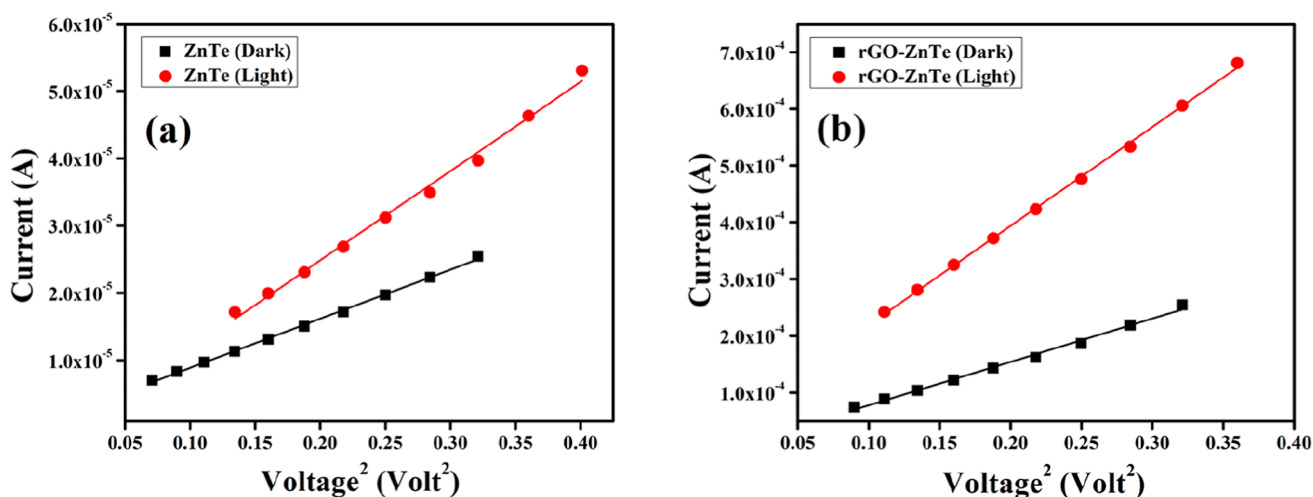| sample		conductivity (σ) (S m^{-1})		mobility (μ_{eff}) (cm^2 V^{-1} s^{-1})		lifetime (τ) (s)	
condition	photosensitivity	dark	light	dark	light	dark	light
ZT	1.75	4.36×10^{-5}	5.71×10^{-5}	3.56×10^{-3}	6.49×10^{-3}	2.91×10^{-6}	1.81×10^{-6}
R−ZT	2.24	3.96×10^{-4}	1.07×10^{-3}	3.54×10^{-2}	8.13×10^{-2}	3.11×10^{-7}	1.39×10^{-7}

Figure 10. Current (I) vs voltage^2 (V^2) plot for the SCLC region for (a) ZT and (b) R−ZT composite.

conductor theory. For this purpose, the $\log(I)$ against $\log(V)$ for positive voltages are plotted in Figure 9b, wherein three distinct linear regions can be delineated implying different conduction mechanisms. Mainly, in a metal−semiconductor junction, the interfacial trap states alter the conduction of charge carriers and thus reform the I−V characteristic curves. At low bias (region-I), the Ohmic behavior ($I \propto V$) with a slope close to unity is observed. In this region, the current is mainly driven by the charge carriers that are intrinsic to the material under investigation.[38] Moving on to region II in Figure 9b, the injected carriers from the contacts are spread over the intrinsic ones for intermediate potential difference values, and they develop a spatially distributed charge field. The charge carriers are then governed by this field, and their "mobility" predominantly controls the quadratic current ($I \propto V^2$) in this region.[39] Finally, for even higher applied voltages,

the device surpasses the trap-filled limit when the injection level of electrons is so high that the conduction is due to the "trap-free space-charge-limited current" followed by the power law ($I \propto V^n$, where $n > 2$) and that this corresponds to region III in Figure 9b.[39b]

To obtain a better understanding of the charge transport mechanism, the I−V characteristics were further analyzed by deciphering the effective carrier's mobility (μ_{eff}) and lifetime (τ) from region II (Figure 9b) based on the space-charge-limited current (SCLC) theory.[39a] The mobility of electrons was estimated from the slope of the I versus V^2 plot (Figure 10a and 10b) according to the Mott−Gurney equation[39b]

$$I = \frac{9\mu_{eff}\varepsilon_0\varepsilon_r A_{eff}}{8}\left(\frac{V^2}{d^3}\right)$$
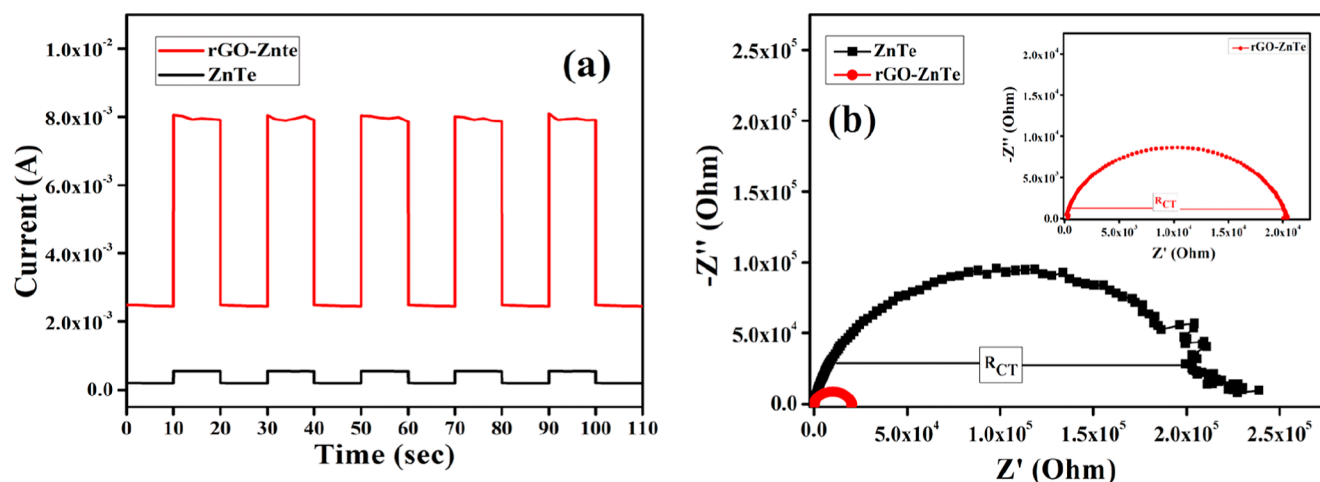
(1)

Figure 11. (a) Transient photocurrent response and (b) EIS Nyquist plots of the pristine ZT and R−ZT composite (inset).
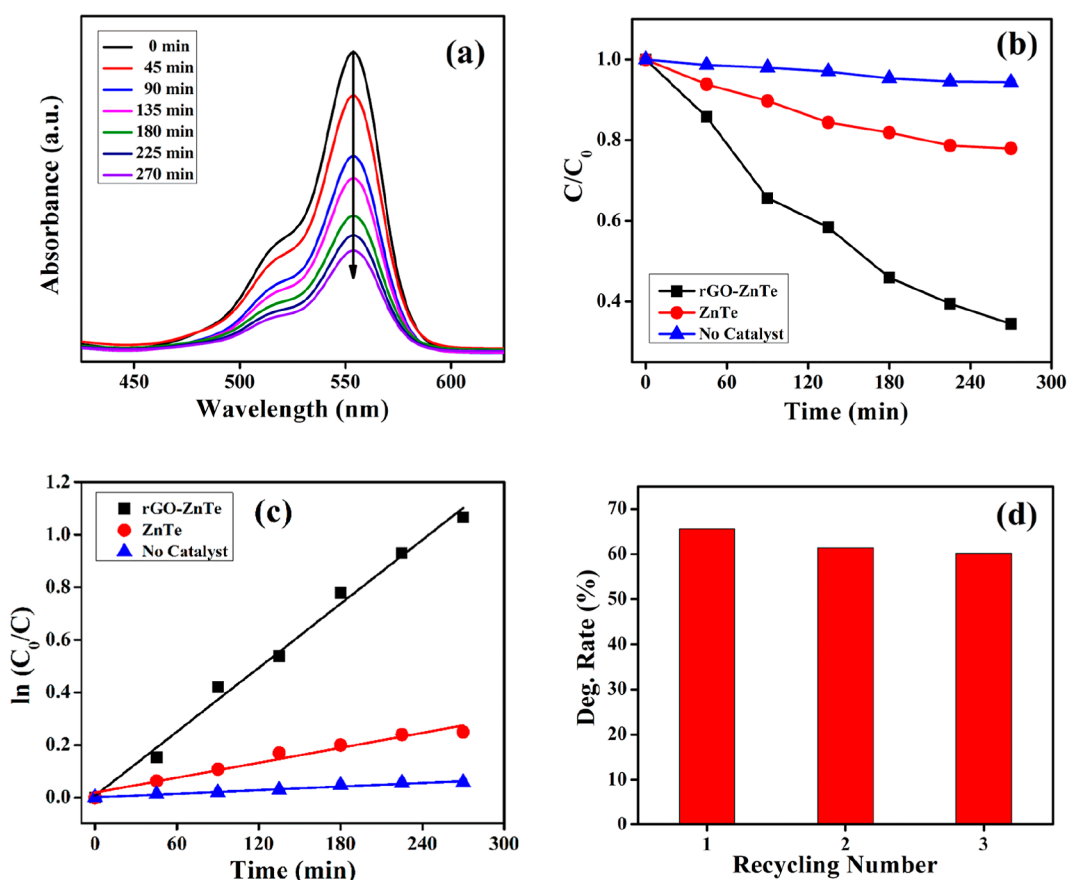

Figure 12. (a) Absorption spectra of aqueous RhB solution for different time intervals in the presence of the R−ZT nanocomposite under the solar simulator. (b) Photocatalytic decomposition behavior and (c) plot of $\ln(C_0/C)$ vs irradiation time for RhB solution in the presence of different catalysts. (d) Recycling performance of the R−ZT catalyst for RhB degradation.

where A_{eff}, ε_0, ε_r, and d stand for the effective diode area, the free space permittivity, the dielectric constant of materials and the thickness of the diode, respectively. The value of the dielectric constant of synthesized materials was estimated from the capacitance (C) versus frequency (f) plot and is discussed in the Supporting Information. Also, the lifetime or transient time (τ) of the charge carriers was extracted employing the following equation[40]

$$\tau = \frac{9\varepsilon_0\varepsilon_r A_{eff}}{8d}\left(\frac{V}{I}\right) \tag{2}$$

The estimated values of μ_{eff} and τ are also presented in Table 1. The higher mobility of graphene and its impressive contribution to the smooth transfer of charge carriers were portrayed in our results. The graphene-based composite exhibited better carrier mobility and lifetime than the as-synthesized ZT nanoparticles. The results are consistent with the previously reported data for the rGO-based inorganic

composite.[18,41] For both dark and light conditions, the mobility of the carriers was significantly increased by almost 10−12 times (Table 1). This enrichment in mobility and in lifetime could enhance the charge transfer efficiency and thus the photocatalytic activity.

To investigate the photo-electrochemical properties of the as-prepared catalysts, the transient photo-response spectra and electrochemical impedance spectroscopy (EIS) Nyquist plots were obtained and are displayed in Figure 11a,b, respectively.[42] As expected, the photocurrent intensity of the R−ZT composite was found to be much higher than that of the pristine ZT. This result indicates that the incorporation of rGO into the ZT nanoparticles could facilitate the separation of the photo-generated electrons and holes and their swift transfer through the 2D graphene channels.[43] Furthermore, the EIS Nyquist spectra, which is also a powerful tool to investigate the conductance and charge transfer facility, showed a much smaller diameter of the semi-circular arc for the R−ZT composite than for the pristine ZT (Figure 11b). This result affirms that the introduction of rGO significantly decreased the charge transfer resistance in the composite material, facilitating the migration of electrons and holes to the active sites during the degradation process, as discussed below.[4b,44]

Photocatalytic Activity. The photocatalytic degradation of RhB under simulated solar light irradiation is used to study the photocatalytic behavior of the pristine ZT and R−ZT nanocomposite. The degradation process was studied by monitoring the major absorption peak of RhB aqueous solution centered at 553.5 nm with the help of a UV−vis spectrometer (Figure 12a), and the degradation process was analyzed using the following equation

$$\text{degradation} = \left(\frac{C_0 - C_t}{C_0} \times 100 \right) \times \% \tag{3}$$

where C_0 and C_t represent the concentration of RhB at the time zero and "t", respectively.[45] The linearity of the $\ln(C_0/C)$ versus illumination time (min) (Figure 12c) for both the pure ZT and R−ZT composite demonstrates the existence of pseudo-first-order degradation kinetics.[46] Under solar light irradiation for 270 min, no considerable change in the RhB concentrations was observed for catalyst-free suspensions. After adding the pure ZT catalyst, the RhB solution was found to be bleached up to 23% of its initial concentration. On the other hand, the R−ZT nanocomposite exhibited an enhanced degradation of 66% due to the synergistic effect of ZT nanoparticles and rGO (Figure 12b). Furthermore, the recycling test (Figure 12d) showed that the degradation efficiency of the R−ZT catalyst does not change conspicuously even after repetitive usage for up to three cycles.

The reactive species in the photocatalytic degradation process were identified by the in situ capture experiments. In these tests, isopropyl alcohol (IPA), disodium ethylenediami-netetraacetate (EDTA-Na$_2$) and N$_2$ atmosphere were used as scavengers in the degradation process. The absorption plots of the degraded RhB by R−ZT in the presence of different scavengers are shown in Figure S6 (Supporting Information). The role of the active species was determined from the variation of C/C_0 with irradiation time (Figure 13) of RhB after the scavengers were added to the photocatalytic system.[47]

As seen in Figure 13, the RhB solution degraded up to 45% of its initial concentration for 270 min irradiation time. It demonstrates that the decomposition of RhB was slightly
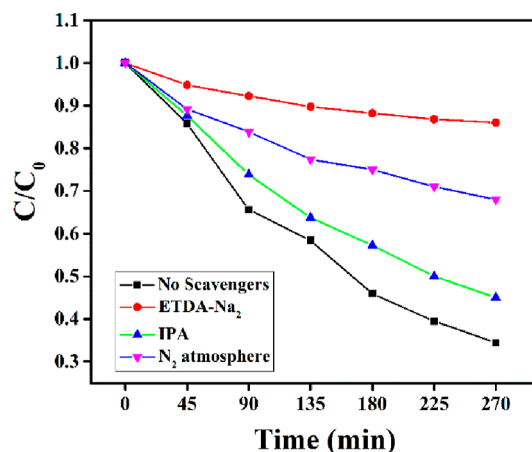

Figure 13. Photocatalytic degradation of RhB aqueous solution by R−ZT in the presence of IPA, EDTA-Na$_2$, N$_2$ atmosphere, and no scavengers.

suppressed in the presence of IPA, a hydroxyl (OH$^\bullet$) quencher, as compared to 34% in the absence of scavengers. This finding indicates that OH$^\bullet$ has a mild effect on photocatalytic degradation of RhB using the R−ZT catalyst. In the case of EDTA-Na$_2$, a quencher of h$^+$, the value of C/C_0 was not reduced below 86%, indicating that holes play a significant role in the RhB degradation. On the other hand, the normalized concentration (C/C_0) was moderately diminished up to 68% when the reaction was carried out in a N$_2$ atmosphere, a quencher of O$_2^{\bullet-}$. This suggests that the O$_2^{\bullet-}$ radical is also markedly responsible for the photocatalytic degradation of RhB. The above-mentioned observations suggest that although all the reactive species contribute to some extent, h$^+$ and O$_2^{\bullet-}$ radicals play a pivotal role in the photodegradation of RhB.[48]

To explain the synergy between rGO and ZT in the composite material, the photocatalytic decomposition process was analyzed. Under visible light irradiation, interfacial excitons originated over the surface of ZT nanoparticles and subsequently separated into free electrons and holes in the conduction band (CB) and valence band (VB), respectively. However, these photogenerated electrons and holes tend to recombine before appearing at the active sites, and thus, a poor photocatalytic reaction is observed. When ZT nanoparticles are attached to the rGO, the photoinduced electron in the CB of ZT could be efficiently separated at the graphene interface leaving behind a hole in the VB of ZT due to their preferable energy levels (Scheme 2).[31,49] Thus, the photogenerated

Scheme 2. Plausible Mechanism of the Photocatalytic Degradation Process of RhB Containing the R−ZT Catalyst under Solar Light Irradiation
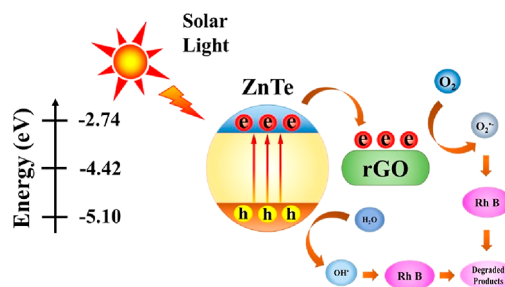
electrons in ZT can easily reach the active sites through the rGO platform and reduce dissolved O_2 present in the aqueous medium to generate the highly reactive superoxide radical anion ($O_2^{\bullet-}$), which can further react with H_2O to form the hydroxyl ($OH^{\bullet}$) radical.[50] Meanwhile, the photoinduced holes may also react with H_2O or OH^- and oxidize them into $OH^{\bullet}$.[51] These $O_2^{\bullet-}$, $OH^{\bullet}$, and the photogenerated holes cooperatively participate in the decomposition process of RhB solution.[52] A schematic representation of the photocatalytic activity of the R–ZT photocatalysts is displayed in Scheme 2.

CONCLUSIONS

The ZT nanoparticles were successfully synthesized, and the incorporation of the rGO sheet with ZT was supported by XRD, TEM, FESEM, XPS, PL and UV–vis spectroscopic data. The charge transport dynamics and the significance of higher carrier mobility of the photocatalysts in the degradation of RhB were studied. The graphene composite exhibited relatively higher photocatalytic activity than the bare ZT under visible light irradiation. The higher mobility of the graphene-based composite material assisted the photoinduced charges in swiftly traveling between active sites and target molecules during the degradation process. The strong interfacial contact along with higher visible light absorption and low electron–hole pair recombination mainly contributed to the enhanced photocatalytic performance of the composite materials. Conclusively, our findings have shed light upon the design and the charge transfer mechanism of the graphene-semi-conductor-based R–ZT composite material, which could be a promising photocatalyst finding diversified applications in wastewater treatment.

ASSOCIATED CONTENT

Ⓢ Supporting Information

The Supporting Information is available free of charge at https://pubs.acs.org/doi/10.1021/acsomega.2c02472.

> Fabrication of the devices, XRD spectra of GO and rGO, calculation of the optical band gap, calculation of the dielectric constant, adsorption profiles of aqueous RhB solution on the pristine ZT and the R–ZT composite as a function of time in the dark, changes in concentration versus time and $\ln(C_0/C)$ versus time plot in the presence of different catalysts under visible light irradiation, and UV–vis absorption spectra of degraded RhB aqueous solution by R–ZT in the presence of isopropyl alcohol, EDTA-Na_2, N_2 atmosphere, and no scavengers (PDF)

AUTHOR INFORMATION

Corresponding Author

Partha Pratim Ray – *Department of Physics, Jadavpur University, Kolkata 700032, India;* ⓘ orcid.org/0000-0003-4616-2577; Phone: +91-9475237259; Email: parthapray@yahoo.com

Authors

Dhananjoy Das – *Department of Physics, Jadavpur University, Kolkata 700032, India*

Mainak Das – *Department of Physics, Jadavpur University, Kolkata 700032, India*

Sayantan Sil – *Department of Physics, University of Engineering and Management, Kolkata 700160, India*

Puspendu Sahu – *Department of Physics, Jadavpur University, Kolkata 700032, India*

Complete contact information is available at:
https://pubs.acs.org/10.1021/acsomega.2c02472

Author Contributions

§D.D., M.D., S.S., P.S., and P.P.R. contributed equally.

Notes

The authors declare no competing financial interest.

ACKNOWLEDGMENTS

ABBREVIATIONS

ZnTe, zinc telluride; GO, graphene oxide; rGO, reduced graphene oxide; rGO–ZnTe, reduced graphene oxide–zinc telluride; HT, hydrothermal; I–V, current–voltage; RhB, Rhodamine B; DI, deionized

REFERENCES

(1) Al-Tohamy, R.; Ali, S. S.; Li, F.; Okasha, K. M.; Mahmoud, Y. A.-G.; Elsamahy, T.; Jiao, H.; Fu, Y.; Sun, J. A critical review on the treatment of dye-containing wastewater: Ecotoxicological and health concerns of textile dyes and possible remediation approaches for environmental safety. *Ecotoxicol. Environ. Saf.* **2022**, *231*, 113160.

(2) Selvaraj, V.; Swarna Karthika, T.; Mansiya, C.; Alagar, M. An over review on recently developed techniques, mechanisms and intermediate involved in the advanced azo dye degradation for industrial applications. *J. Mol. Struct.* **2021**, *1224*, 129195.

(3) Liu, D.; Li, C.; Zhao, C.; Zhao, Q.; Niu, T.; Pan, L.; Xu, P.; Zhang, F.; Wu, W.; Ni, T. Facile synthesis of three-dimensional hollow porous carbon doped polymeric carbon nitride with highly efficient photocatalytic performance. *Chem. Eng. J. (Amsterdam, Neth.)* **2022**, *438*, 135623.

(4) (a) Zhao, Y.; Li, R.; Mu, L.; Li, C. Significance of crystal morphology controlling in semiconductor-based photocatalysis: a case study on BiVO4 photocatalyst. *Cryst. Growth Des.* **2017**, *17*, 2923–2928. (b) Ni, T.; Yang, Z.; Zhang, H.; Zhou, L.; Guo, W.; Pan, L.; Yang, Z.; Chang, K.; Ge, C.; Liu, D. Peroxymonosulfate activation by Co3O4/SnO2 for efficient degradation of ofloxacin under visible light. *J. Colloid Interface Sci.* **2022**, *615*, 650–662.

(5) Zhang, Z.; Wang, W.; Wang, L.; Sun, S. Enhancement of Visible-Light Photocatalysis by Coupling with Narrow-Band-Gap Semiconductor: A Case Study on Bi2S3/Bi2WO6. *ACS Appl. Mater. Interfaces* **2012**, *4*, 593–597.

(6) (a) Akpan, U. G.; Hameed, B. H. Parameters affecting the photocatalytic degradation of dyes using TiO2-based photocatalysts: A review. *J. Hazard. Mater.* **2009**, *170*, 520–529. (b) Liu, D.; Li, H.; Gao, R.; Zhao, Q.; Yang, Z.; Gao, X.; Wang, Z.; Zhang, F.; Wu, W. Enhanced visible light photoelectrocatalytic degradation of tetracycline hydrochloride by I and P co-doped TiO2 photoelectrode. *J. Hazard. Mater.* **2021**, *406*, 124309.

(7) Aarthi, T.; Madras, G. Photocatalytic degradation of rhodamine dyes with nano-TiO2. *Ind. Eng. Chem. Res.* **2007**, *46*, 7−14.

(8) Lee, K. S.; Oh, G.; Kim, E. K. High performance intermediate-band solar cells based on ZnTe:Cr with ZnO:Al electron transport layer. *Sol. Energy* **2018**, *164*, 262−266.

(9) Son, M.; Kim, S.; Lee, Y.; Bang, J. Synthesis of near-infrared-emitting type-II In(Zn)P/ZnTe (core/shell) quantum dots. *J. Alloys Compd.* **2021**, *886*, 161233.

(10) Olusola, O. I.; Oluyamo, S. S.; Ajayi, O. A. Opto-electronic properties of electrodeposited ZnTe using zinc anode as counter electrode. *Mater. Sci. Semicond. Process.* **2021**, *123*, 105494.

(11) Ehsan, M. F.; Ashiq, M. N.; He, T. Hollow and mesoporous ZnTe microspheres: synthesis and visible-light photocatalytic reduction of carbon dioxide into methane. *RSC Adv.* **2015**, *5*, 6186−6194.

(12) (a) Wu, X.-P.; Gu, J.; Zhou, S.-M.; Li, X.-Y.; Wang, S.-L.; Jin, L.; Chen, H.; Shi, J.-J. Red bayberry-like ZnTe microstructures: controlled synthesis, growth mechanism and enhanced photocatalytic performance. *J. Alloys Compd.* **2015**, *627*, 166−173. (b) Sun, Y.; Zhao, Q.; Gao, J.; Ye, Y.; Wang, W.; Zhu, R.; Xu, J.; Chen, L.; Yang, J.; Dai, L.; Liao, Z.-m.; Yu, D. In situ growth, structure characterization, and enhanced photocatalysis of high-quality, single-crystalline ZnTe/ZnO branched nanoheterostructures. *Nanoscale* **2011**, *3*, 4418−4426. (c) Raza, N.; Raza, W.; Gul, H.; Kim, K.-H. ZnO−ZnTe hierarchical superstructures as solar-light-activated photocatalysts for azo dye removal. *Environ. Res.* **2021**, *194*, 110499.

(13) (a) Sun, H.; Liu, S.; Zhou, G.; Ang, H. M.; Tadé, M. O.; Wang, S. Reduced Graphene Oxide for Catalytic Oxidation of Aqueous Organic Pollutants. *ACS Appl. Mater. Interfaces* **2012**, *4*, 5466−5471. (b) Thakur, K.; Kandasubramanian, B. Graphene and Graphene Oxide-Based Composites for Removal of Organic Pollutants: A Review. *J. Chem. Eng. Data* **2019**, *64*, 833−867.

(14) (a) Saxena, S.; Tyson, T. A.; Shukla, S.; Negusse, E.; Chen, H.; Bai, J. Investigation of structural and electronic properties of graphene oxide. *Appl. Phys. Lett.* **2011**, *99*, 013104. (b) Li, D.; Müller, M. B.; Gilje, S.; Kaner, R. B.; Wallace, G. G. Processable aqueous dispersions of graphene nanosheets. *Nat. Nanotechnol.* **2008**, *3*, 101−105. (c) Liu, W.; Cai, J.; Li, Z. Self-assembly of semiconductor nanoparticles/reduced graphene oxide (RGO) composite aerogels for enhanced photocatalytic performance and facile recycling in aqueous photocatalysis. *ACS Sustainable Chem. Eng.* **2015**, *3*, 277−282.

(15) Liu, B.; Liu, X.; Liu, J.; Feng, C.; Li, Z.; Li, C.; Gong, Y.; Pan, L.; Xu, S.; Sun, C. Q. Efficient charge separation between UiO-66 and ZnIn2S4 flowerlike 3D microspheres for photoelectronchemical properties. *Appl. Catal., B* **2018**, *226*, 234−241.

(16) (a) Wang, B. B.; Zhu, M. K.; Wang, H.; Dong, G. B. Study on growth and photoluminescence of zinc telluride crystals synthesized by hydrothermal method. *Opt. Mater.* **2011**, *34*, 42−47. (b) Ehsan, M. F.; Ashiq, M. N.; Bi, F.; Bi, Y.; Palanisamy, S.; He, T. Preparation and characterization of SrTiO 3−ZnTe nanocomposites for the visible-light photoconversion of carbon dioxide to methane. *RSC Adv.* **2014**, *4*, 48411−48418.

(17) (a) Hummers, W. S., Jr.; Offeman, R. E. Preparation of graphitic oxide. *J. Am. Chem. Soc.* **1958**, *80*, 1339. (b) Marcano, D. C.; Kosynkin, D. V.; Berlin, J. M.; Sinitskii, A.; Sun, Z.; Slesarev, A.; Alemany, L. B.; Lu, W.; Tour, J. M. Improved synthesis of graphene oxide. *ACS Nano* **2010**, *4*, 4806−4814.

(18) Das, M.; Datta, J.; Dey, A.; Jana, R.; Layek, A.; Middya, S.; Ray, P. P. One step hydrothermal synthesis of a rGO−TiO 2 nano-composite and its application on a Schottky diode: improvement in device performance and transport properties. *RSC Adv.* **2015**, *5*, 101582−101592.

(19) Perera, S. D.; Mariano, R. G.; Vu, K.; Nour, N.; Seitz, O.; Chabal, Y.; Balkus, K. J., Jr Hydrothermal synthesis of graphene-TiO2 nanotube composites with enhanced photocatalytic activity. *ACS Catal.* **2012**, *2*, 949−956.

(20) Rietveld, H. M. A profile refinement method for nuclear and magnetic structures. *J. Appl. Crystallogr.* **1969**, *2*, 65−71.

(21) Holland, H. J.; Beck, K. Thermal Expansion of Zinc Telluride from 0° to 460°C. *J. Appl. Phys.* **1968**, *39*, 3498−3499.

(22) (a) Meng, Q.; Jiang, C.; Mao, S. X. Temperature-dependent growth of zinc-blende-structured ZnTe nanostructures. *J. Cryst. Growth* **2008**, *310*, 4481−4486. (b) Wang, B. B.; Zhu, M. K.; Wang, H.; Dong, G. B.; Xie, H. L. Study on effects of sodium hydroxide on synthesis of zinc telluride nanocrystals by hydrothermal method. *Mater. Sci. Semicond. Process.* **2012**, *15*, 131−135. (c) Wang, B. B.; Xu, X. Z. Study on effects of time and temperature on growth of nanocrystalline zinc selenide synthesized by hydrothermal method. *J. Cryst. Growth* **2009**, *311*, 4759−4762.

(23) Chen, Y.-L.; Hu, Z.-A.; Chang, Y.-Q.; Wang, H.-W.; Zhang, Z.-Y.; Yang, Y.-Y.; Wu, H.-Y. Zinc oxide/reduced graphene oxide composites and electrochemical capacitance enhanced by homogeneous incorporation of reduced graphene oxide sheets in zinc oxide matrix. *J. Phys. Chem. C* **2011**, *115*, 2563−2571.

(24) Zhang, J.; Sun, K.; Kumbhar, A.; Fang, J. Shape-control of ZnTe nanocrystal growth in organic solution. *J. Phys. Chem. C* **2008**, *112*, 5454−5458.

(25) Pan, S.; Liu, X. ZnS−Graphene nanocomposite: Synthesis, characterization and optical properties. *J. Solid State Chem.* **2012**, *191*, 51−56.

(26) Xu, C.; Wang, X.; Zhu, J. Graphene−metal particle nano-composites. *J. Phys. Chem. C* **2008**, *112*, 19841−19845.

(27) (a) Li, Q.; Guo, B.; Yu, J.; Ran, J.; Zhang, B.; Yan, H.; Gong, J. R. Highly efficient visible-light-driven photocatalytic hydrogen production of CdS-cluster-decorated graphene nanosheets. *J. Am. Chem. Soc.* **2011**, *133*, 10878−10884. (b) Gao, M.; Wu, X.; Qiu, H.; Zhang, Q.; Huang, K.; Feng, S.; Yang, Y.; Wang, T.; Zhao, B.; Liu, Z. Reduced graphene oxide-mediated synthesis of Mn 3O4 nanomaterials for an asymmetric supercapacitor cell. *RSC Adv.* **2018**, *8*, 20661−20668.

(28) (a) Kang, Z. T.; Menkara, H.; Wagner, B. K.; Summers, C. J.; Durst, R.; Diawara, Y.; Mednikova, G.; Thorson, T. Effects of annealing atmosphere on the luminescent efficiency of ZnTe: O phosphors. *J. Lumin.* **2006**, *117*, 156−162. (b) Potlog, T.; Duca, D.; Dobromir, M. Temperature-dependent growth and XPS of Ag-doped ZnTe thin films deposited by close space sublimation method. *Appl. Surf. Sci.* **2015**, *352*, 33−37.

(29) Baghchesara, M. A.; Cheraghizade, M.; Yousefi, R. Growth and characterization of ZnTe nanowires grown in a large scale by a CVD method. *Mater. Lett.* **2016**, *162*, 195−198.

(30) Tauc, J.; Grigorovici, R.; Vancu, A. Optical properties and electronic structure of amorphous germanium. *Phys. Status Solidi B* **1966**, *15*, 627−637.

(31) Rawalekar, S.; Kaniyankandy, S.; Verma, S.; Ghosh, H. N. Effect of surface states on charge-transfer dynamics in type II CdTe/ZnTe Core−shell quantum dots: A femtosecond transient absorption study. *J. Phys. Chem. C* **2011**, *115*, 12335−12342.

(32) (a) Cheng, T.; Li, D.; Li, J.; Ren, B.; Wang, G.; Cheng, J. Aqueous synthesis of high-fluorescence ZnTe quantum dots. *J. Mater. Sci.: Mater. Electron.* **2015**, *26*, 4062−4068. (b) Wang, H.-X.; Wu, R.; Wei, S.-H.; Yu, L.-R.; Jian, J.-K.; Hou, J.; Wang, J.; Zhang, H.-Y.; Sun, Y.-F. One-pot solvothermal synthesis of ZnTe/RGO nanocomposites and enhanced visible-light photocatalysis. *Chin. Chem. Lett.* **2016**, *27*, 1572−1576.

(33) (a) Chen, Z.; Berciaud, S.; Nuckolls, C.; Heinz, T. F.; Brus, L. E. Energy transfer from individual semiconductor nanocrystals to graphene. *ACS Nano* **2010**, *4*, 2964−2968. (b) Kumar, S.; Surendar, T.; Baruah, A.; Shanker, V. Synthesis of a novel and stable gC 3 N 4−Ag 3 PO 4 hybrid nanocomposite photocatalyst and study of the photocatalytic activity under visible light irradiation. *J. Mater. Chem. A* **2013**, *1*, 5333−5340.

(34) Wan, B.; Hu, C.; Feng, B.; Xu, J.; Zhang, Y.; Tian, Y. Optical properties of ZnTe nanorods synthesized via a facile low-temperature solvothermal route. *Mater. Sci. Eng. B* **2010**, *171*, 11−15.

(35) Madhusudan, P.; Zhang, J.; Cheng, B.; Liu, G. Photocatalytic degradation of organic dyes with hierarchical Bi 2 O 2 CO 3

microstructures under visible-light. *CrystEngComm* **2013**, *15*, 231−240.

(36) Yang, Q.; Guo, X.; Wang, W.; Zhang, Y.; Xu, S.; Lien, D. H.; Wang, Z. L. Enhancing sensitivity of a single ZnO micro-/nanowire photodetector by piezo-phototronic effect. *ACS Nano* **2010**, *4*, 6285−6291.

(37) Sun, S.; Gao, L.; Liu, Y. Enhanced dye-sensitized solar cell using graphene-TiO 2 photoanode prepared by heterogeneous coagulation. *Appl. Phys. Lett.* **2010**, *96*, 083113.

(38) Taşçıoğlu, İ.; Aydemir, U.; Altındal, Ş. The explanation of barrier height inhomogeneities in Au/n-Si Schottky barrier diodes with organic thin interfacial layer. *J. Appl. Phys.* **2010**, *108*, 064506.

(39) (a) Ullah, I.; Shah, M.; Khan, M.; Wahab, F. Consistency in Al/CuPc/n-Si Heterojunction Diode Parameters Extracted Using Different Techniques. *J. Electron. Mater.* **2016**, *45*, 1175−1183. (b) Soylu, M.; Abay, B. Analysing space charge-limited conduction in Au/n-InP Schottky diodes. *Phys. E* **2010**, *43*, 534−538.

(40) Sil, S.; Dey, A.; Datta, J.; Das, M.; Jana, R.; Halder, S.; Dhar, J.; Sanyal, D.; Ray, P. P. Analysis of interfaces in Bornite (Cu5FeS4) fabricated Schottky diode using impedance spectroscopy method and its photosensitive behavior. *Mater. Res. Bull.* **2018**, *106*, 337−345.

(41) Das, M.; Datta, J.; Jana, R.; Sil, S.; Halder, S.; Ray, P. P. Synthesis of rGO−Zn 0.8 Cd 0.2 S via in situ reduction of GO for the realization of a Schottky diode with low barrier height and highly enhanced photoresponsivity. *New J. Chem.* **2017**, *41*, 5476−5486.

(42) Liu, D.; Li, C.; Ni, T.; Gao, R.; Ge, J.; Zhang, F.; Wu, W.; Li, J.; Zhao, Q. 3D interconnected porous g-C3N4 hybridized with Fe2O3 quantum dots for enhanced photo-Fenton performance. *Appl. Surf. Sci.* **2021**, *555*, 149677.

(43) Liu, D.; Li, C.; Ge, J.; Zhao, C.; Zhao, Q.; Zhang, F.; Ni, T.; Wu, W. 3D interconnected g-C3N4 hybridized with 2D Ti3C2 MXene nanosheets for enhancing visible light photocatalytic hydrogen evolution and dye contaminant elimination. *Appl. Surf. Sci.* **2022**, *579*, 152180.

(44) Cheng, T.; Gao, H.; Liu, G.; Pu, Z.; Wang, S.; Yi, Z.; Wu, X.; Yang, H. Preparation of core-shell heterojunction photocatalysts by coating CdS nanoparticles onto Bi4Ti3O12 hierarchical microspheres and their photocatalytic removal of organic pollutants and Cr (VI) ions. *Colloids Surf., A* **2022**, *633*, 127918.

(45) Khanchandani, S.; Kundu, S.; Patra, A.; Ganguli, A. K. Band Gap Tuning of ZnO/In2S3 Core/Shell Nanorod Arrays for Enhanced Visible-Light-Driven Photocatalysis. *J. Phys. Chem. C* **2013**, *117*, 5558−5567.

(46) Herrmann, J.-M. Heterogeneous photocatalysis: fundamentals and applications to the removal of various types of aqueous pollutants. *Catal. Today* **1999**, *53*, 115−129.

(47) Li, L.; Sun, X.; Xian, T.; Gao, H.; Wang, S.; Yi, Z.; Wu, X.; Yang, H. Template-free synthesis of Bi 2 O 2 CO 3 hierarchical nanotubes self-assembled from ordered nanoplates for promising photocatalytic applications. *Phys. Chem. Chem. Phys.* **2022**, *24*, 8279−8295.

(48) Liu, T.; Wang, L.; Lu, X.; Fan, J.; Cai, X.; Gao, B.; Miao, R.; Wang, J.; Lv, Y. Comparative study of the photocatalytic performance for the degradation of different dyes by ZnIn 2 S 4: adsorption, active species, and pathways. *RSC Adv.* **2017**, *7*, 12292−12300.

(49) Padhi, D. K.; Parida, K. Facile fabrication of α-FeOOH nanorod/RGO composite: a robust photocatalyst for reduction of Cr(vi) under visible light irradiation. *J. Mater. Chem. A* **2014**, *2*, 10300−10312.

(50) Huang, L.; Peng, F.; Yu, H.; Wang, H. Preparation of cuprous oxides with different sizes and their behaviors of adsorption, visible-light driven photocatalysis and photocorrosion. *Solid State Sci.* **2009**, *11*, 129−138.

(51) Wang, M.; Sun, L.; Lin, Z.; Cai, J.; Xie, K.; Lin, C. p−n Heterojunction photoelectrodes composed of Cu2O-loaded TiO2 nanotube arrays with enhanced photoelectrochemical and photoelectrocatalytic activities. *Energy Environ. Sci.* **2013**, *6*, 1211−1220.

(52) (a) Wang, H.; Wu, Y.; Wu, P.; Chen, S.; Guo, X.; Meng, G.; Peng, B.; Wu, J.; Liu, Z. Environmentally benign chitosan as reductant and supporter for synthesis of Ag/AgCl/chitosan composites by one-step and their photocatalytic degradation performance under visible-light irradiation. *Front. Mater. Sci.* **2017**, *11*, 130−138. (b) Zhang, Z.; Zhai, S.; Wang, M.; Ji, H.; He, L.; Ye, C.; Wang, C.; Fang, S.; Zhang, H. Photocatalytic degradation of rhodamine B by using a nanocomposite of cuprous oxide, three-dimensional reduced graphene oxide, and nanochitosan prepared via one-pot synthesis. *J. Alloys Compd.* **2016**, *659*, 101−111.